Physica Medica 99 (2022) 61–67

Contents lists available at ScienceDirect

Physica Medica

journal homepage: www.elsevier.com/locate/ejmp

Original paper

A tin filter's dose reduction effect revisited: Using the detectability index in low-dose computed tomography for the chest

Akira Hasegawa [a,b], Katsuhiro Ichikawa [c,*], Yusuke Morioka [b,d], Hiroki Kawashima [c]

[a] Department of Radiological Technology, Faculty of Medical Technology, Niigata University of Health and Welfare, 1398 Shimami-cho, Kita-ku, Niigata-shi, Niigata 950-3198, Japan
[b] Graduate School of Medical Science, Kanazawa University, 5-11-80 Kodatsuno, Kanazawa, Ishikawa 920-0942, Japan
[c] Faculty of Health Sciences, Institute of Medical, Pharmaceutical and Health Sciences, Kanazawa University, 5-11-80 Kodatsuno, Kanazawa, Ishikawa 920-0942, Japan
[d] Department of Radiology, Toyama Prefectural Central Hospital, 2-2-78, Nishinagae, Toyama-shi, Toyama 930-8550, Japan

ARTICLE INFO

Keywords:
Chest computed tomography
Tin filter
Radiation dose
Detectability index

ABSTRACT

Purpose: To reevaluate a tin filter's (TF) dose reduction effect in computed tomography (CT) using a combination of an anthropomorphic chest phantom and a rod-shaped phantom.
Methods and materials: A third-generation dual-source CT system equipped with a built-in TF was employed. A chest phantom was scanned under low-dose conditions of 0.2 to 1.0 mGy with the TF at 100 kV (TF100kV) and without it at 100 kV and 120 kV (NF100kV and NF120kV). To eliminate effects other than that of the TF, only filtered back projection (FBP) was used for image reconstruction. On the images of the rod phantom placed inside the lung field, the CT number and the spatial resolution using the modulation transfer function (MTF) were measured. Using these indices plus the noise power spectrum (NPS) that was also measured, the detectability index based on the non-prewhitening model observer (d'_{NPW}) was calculated.
Results: The CT numbers and MTFs were almost identical across the three conditions. The area under the NPS curve was decreased by 13–17% with the TF compared with non-TF conditions. NPS increases at low frequencies of < 0.06 mm^{-1} observed in NF120kV and NF100kV were eliminated by TF100kV. The potential dose reduction by the TF, estimated using the d'_{NPW} values, turned out to be 22 to 25%.
Conclusion: Based on the analysis of the FBP images of a chest phantom, the dose reduction attributable only to the TF was estimated at 22–25%, notably lower than those reported in previous studies.

Introduction

The cancer risk associated with high amounts of radiation dose during a computed tomography (CT) scan is a serious concern [1]. Accordingly, CT vendors are constantly developing tools and methods for reducing the dose required for CT acquisition while mitigating its influence on image quality. The additional built-in tin filter (TF) is one of such tools: It absorbs low-energy photons, which tend to increase the dose to the patient without contributing to image quality, more aggressively than other filters used in conventional X-ray CT systems [2]. Because of this aggressive low-energy photon absorption, the X-ray beam is hardened by the TF, thereby increasing the effective energy. Therefore, contrast-enhanced protocols are not selected as applications of the TF. Even at 100 kV instead of a conventional 120 kV, a contrast reduction by the TF is inevitable [2]. Therefore, combined with demands for low-dose acquisition in chest CT screening, clinical studies using this filter have focused on non-contrast-enhanced chest CT [3–8]; the results of most studies have indicated that the radiation dose was significantly lower with protocols with a TF than with conventional protocols without a TF. However, one study for pediatric chest CT reports that the clinical performance was not significantly different between cases with and without a TF at the same radiation dose [8]. The majority of studies preceding to it had reported that significant dose reductions attributable to a TF were made between different CT systems with and without a TF; iterative reconstruction (IR) methods used were also different between the CT systems [3,4,6,7]. Furthermore, variations in physical image

* Corresponding author at: Faculty of Health Sciences, Institute of Medical, Pharmaceutical and Health Sciences, Kanazawa University, 5-11-80 Kodatsuno, Kanazawa, Ishikawa 920-0942, Japan.
E-mail addresses: akira-hasegawa@nuhw.ac.jp (A. Hasegawa), ichikawa@mhs.mp.kanazawa-u.ac.jp (K. Ichikawa), equitess1869@hotmail.co.jp (Y. Morioka), kawa3@med.kanazawa-u.ac.jp (H. Kawashima).

https://doi.org/10.1016/j.ejmp.2022.05.006
Received 30 January 2022; Received in revised form 30 April 2022; Accepted 15 May 2022

quality due to the use of a TF were evaluated only with a phantom simulating an adult abdomen [2]; a numerical simulation investigating the dose reduction potential of TF with a wider range of tube voltages was performed; however, its target was also only abdomen [9]. Thus, it is not prudent to claim that they precisely estimated potential dose reductions for chest CT. Therefore, it has not been clearly explained to date how much a TF alone contributes to the reduction in dose in chest CT.

The purpose of this study is to estimate the potential contribution of a TF to dose reduction, using an anthropomorphic chest phantom in combination with a rod-shaped phantom made of a soft-tissue equivalent material with a precise energy dependency corresponding to the beam hardening by the TF.

Methods and materials

CT system and phantom

A third-generation dual-source CT system, Somatom Force (Siemens Healthineers), equipped with a built-in TF with a thickness of 0.6 mm was employed in this study. An anthropomorphic chest phantom (LSCT001, Kyoto Kagaku, Japan) that simulates an adult chest was used in combination with a custom-made rod-shaped phantom for measuring spatial resolution and the CT number. After removing default parts simulating lung vessels from the chest phantom, the rod-shaped phantom with a diameter of 20 mm and a height of 30 mm, made of a soft-tissue equivalent material (STEM-06, Kyoto Kagaku), was placed inside the right side of air cavities (corresponding to the right lung field) created by the removal of the vessel parts. The locations of the center slice of the rod phantom were 60 mm below the lung apex corresponding to the apical segment in the upper lobe (AS) and 80 mm above the top of right dome of the diaphragm corresponding to the basal segment in the lower lobe (BS) (Fig. 1). The rod phantom was placed such that the rod axis was parallel to the rotation axis of the CT system. The material of STEM-06 provides a photon energy dependency equivalent to that of soft tissue at energies from 40 to 160 keV [10], so that contrast variations due to the beam hardening caused by the TF can be accurately reproduced. One of the purposes of using a rod phantom was to measure its CT number; the other was to measure spatial resolution (modulation transfer function (MTF)) from the circular edge of the cross-section image (disk image) of the rod phantom using the circular edge method described later.

Data acquisition and reconstruction

Scans in single source mode were performed at 100 kV with the TF (TF100kV); 100 kV and 120 kV without it (NF100kV and NF120kV). The tube current was adjusted to achieve volume CT dose index ($CTDI_{vol}$) values of 0.2, 0.4, 0.6, 0.8, and 1.0 mGy. Due to the lower limit of the tube current, the combination of 0.2 mGy at 120 kV was excluded. The other conditions were 0.25 s per rotation, a detector configuration of 0.6 × 192 mm, and a pitch factor of 1.2 in helical mode. The chest phantom including the rod phantom was repeatedly scanned ten times; moreover, the chest phantom without the rod phantom was also scanned ten times for noise power spectrum (NPS) measurement (described later). The CT images were reconstructed with a display field of view (DFOV) of 200 mm, a slice thicknesses of 1.0 mm, a table increment of 1.0 mm, and a reconstruction kernel of Br40. As for the reconstruction algorithm, only filtered back projection (FBP) was employed and IR techniques were excluded because FBP is a linear reconstruction method which can correctly investigate the lone effect of the TF on image quality.

CT number

The CT number of the rod phantom for each of the three conditions (TF100kV, NF120kV, and NF100kV) was measured using a total of 100 images (10 consecutive images at each scan) at 1.0 mGy with a region of interest (ROI) of 32 × 32 pixels. The averaged CT numbers obtained from the 100 images were compared between the three conditions and used to calculate the detectability index as described later.

MTF measurement

Prior to the data processing for MTF calculation, image averaging using the images obtained over the ten acquisitions was performed to improve the accuracy of MTF measurement by reducing the image noise. Only the center slice of the rod phantom was used for averaging because the phantom alignment is precisely identical for all the 10 images. The image contrast of the rod phantom based on the background (air) was very high (>1000 Hounsfield unit [HU]); therefore, the contrast-to-noise ratio of the averaged image clearly satisfied the recommendation (>15) in a guideline [11] even at the lowest dose of 0.2 mGy. MTFs were calculated using the circular edge method previously reported [12–16]. In summary, a one-dimensional (1D) edge spread function (ESF) was synthesized from the circular edge of the averaged cross section image. Then, the ESF was differentiated to produce the line spread function (LSF), followed by a Fourier transform of the LSF to calculate the frequency responses in MTF.

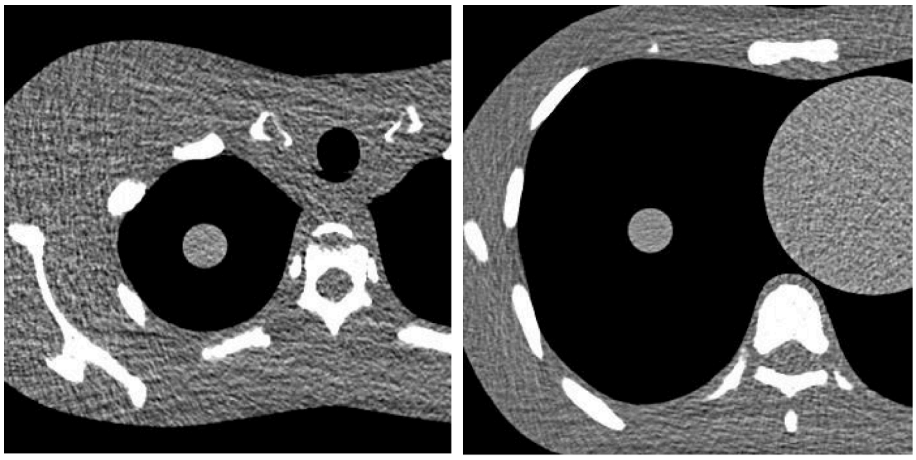

Fig. 1. CT image examples of a chest phantom including a rod-shaped phantom with a window condition for the mediastinum (window width = 500 HU, window center = 30 HU). The rod phantom with a diameter of 20 mm and a height of 30 mm was placed (a) in the right lung field at 60 mm below the lung apex corresponding to the apical segment (AS) in the upper lobe and (b) at 80 mm above the top of right dome of diaphragm corresponding to the basal segment (BS) in the lower lobe.

NPS measurement

The CT images of the chest phantom without the rod phantom were reconstructed for the locations corresponding to the AS and the BS. A total of 200 images (20 consecutive images for one acquisition) were used for the NPS measurement at each location. For an ROI of 128 × 128 pixels (50 × 50 mm) placed in the uniform area of the lung field (air part) of each image, the NPS was calculated. An established method using two-dimensional (2D) Fourier transform was employed [14,16–18]. The NPS results of the 200 images were averaged to minimize the statistical error of the measurement to a negligible level.

Detectability index

We used the detectability index (d') based on the non-prewhitening model observer as a task-specific figure of merit for imaging performance [11,19–21], which is calculated using the following formula:

$$d_{NPW}^2 = \frac{\left[2\pi \int f \cdot W_{task}^2(f) \cdot MTF^2(f) df\right]^2}{2\pi \int f \cdot W_{task}^2(f) \cdot MTF^2(f) \cdot NPS(f) df} \quad (1)$$

where f is the radial frequency and W_{task} is the magnitude of the Fourier transform of the rod image as shown below,

$$W_{task}(f) = \Delta HU \frac{2J_1(\pi \phi f)}{\pi \phi f} \quad (2)$$

where ΔHU is the difference in CT number between the soft-tissue equivalent rod and the air background and J_1 and φ are the First-order Bessel function and the rod diameter, respectively [22,23]. φ was set at 5.0 mm, assuming a small solid nodule. This model observer compares the image of interest to a template consisting of the expected signal using cross-correlation technique, which can be achieved by calculation in the Fourier domain, including W_{task} corresponding to the template, shown in the above equations. This model has been demonstrated to correlate strongly with human performance for low-contrast detection tasks [12]. We assessed the spatial resolution using the MTF rather than the task transfer function (TTF) because we used only FBP (which is linear) as the reconstruction algorithm. Thus, the d'^2_{NPW} in this study depends on W_{task} and NPS. We initially thought of estimating d' values corresponding to a pure grand-glass nodule (GGN) with a diameter of 5 mm and ΔHU = 100–200 HU [24,25]. We decided, however, not to do it because we presumed that relative changes in d' value caused by the TF (i.e., effect of the TF on d') would not be much different between simulations of the solid nodule and the pure GGN. The pure GGN's low CT numbers tend to be due to air in the alveolar structures in it [25]; thus, the rates of CT number change caused by the TF from the CT number without the TF are expected to be the same between the solid nodule and pure GGN because of the no energy dependency of air.

Results

CT number

The averaged CT numbers of the rod phantom at the AS were 58.3, 58.6, and 58.2 HU for TF100kV, NF100kV, and NF120kV, respectively. Those at the BS were 59.6, 62.8, and 61.2 HU, respectively. A slight decrease in CT number caused by the beam hardening with a TF was observed at the BS.

Modulation transfer function

Fig. 2 shows the results of MTF for the AS and the BS at 0.4 mGy. The MTFs were mostly identical. For this dose, the 50%MTFs of TF100kV, NF100kV, and NF120kV were 0.344, 0.336, and 0.333 mm^{-1} at AS, respectively; 0.338, 0.337, and 0.338 mm^{-1} at BS, respectively. Similarly, MTFs were also mostly identical at the other doses.

Noise power spectrum

Fig. 3 shows the results of NPS at 0.4 and 0.8 mGy. The NPSs at the other doses exhibited similar tendencies. Table 1 shows the area under the NPS curve for all the NPSs. Conspicuous differences between TF and NF cases were observed at low spatial frequencies of < 0.06 mm^{-1}, which are greater with NF100kV and NF120kV than with TF100kV. It is suspected that the increases in noise resulted from more streak artifacts observed with NF100kV and NF120kV than with TF100kV. The area under the NPS curve of TF100kV was 13.7–15.9% lower than that of NF100kV and 12.6–16.9% lower than that of NF120kV.

Detectability index

Fig. 4 shows how d'^2_{NPW} varies as a function of radiation dose. For the AS, the percent increases of TF100kV compared with NF120kV ranged from 21.8 (0.6 mGy) to 26.2% (0.4 mGy). Those compared with NF100kV ranged from 22.0 (0.4 mGy) to 28.9% (1.0 mGy). For the BS, the percent increases of TF100kV compared with NF120kV ranged from 18.0 (0.6 mGy) to 23.6% (0.8 mGy). Those compared with NF100kV ranged from 16.4 (0.2 mGy) to 27.5% (1.0 mG). When using TF100kV (by appropriately reducing the dose) as compared with NF120kV at 0.6 mGy, the potential dose reduction was 22% at both the AS and the BS.

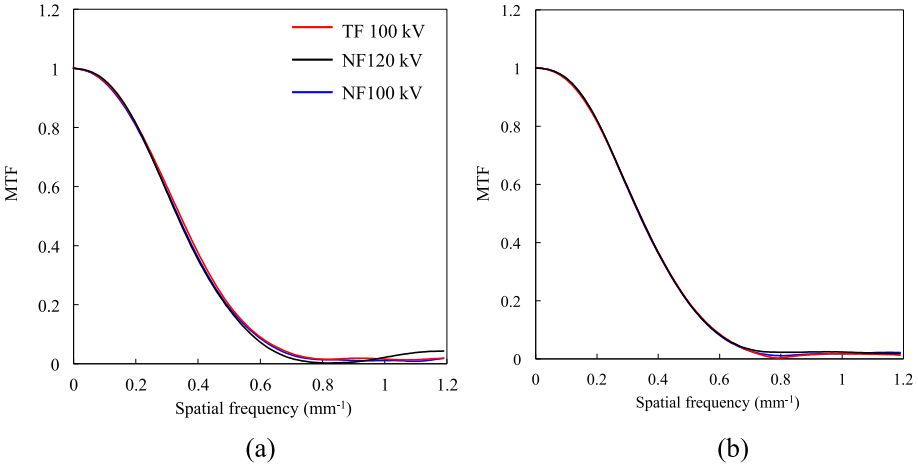

Fig. 2. MTF results for (a) the AS and (b) the BS at 0.4 mGy for 100 kV with the TF (TF100kV); 100 kV and 120 kV without TF (NF100kV and NF120kV). Similarly, MTFs were also mostly identical at the other doses (0.2, 0.6, 0.8, and 1.0 mGy).

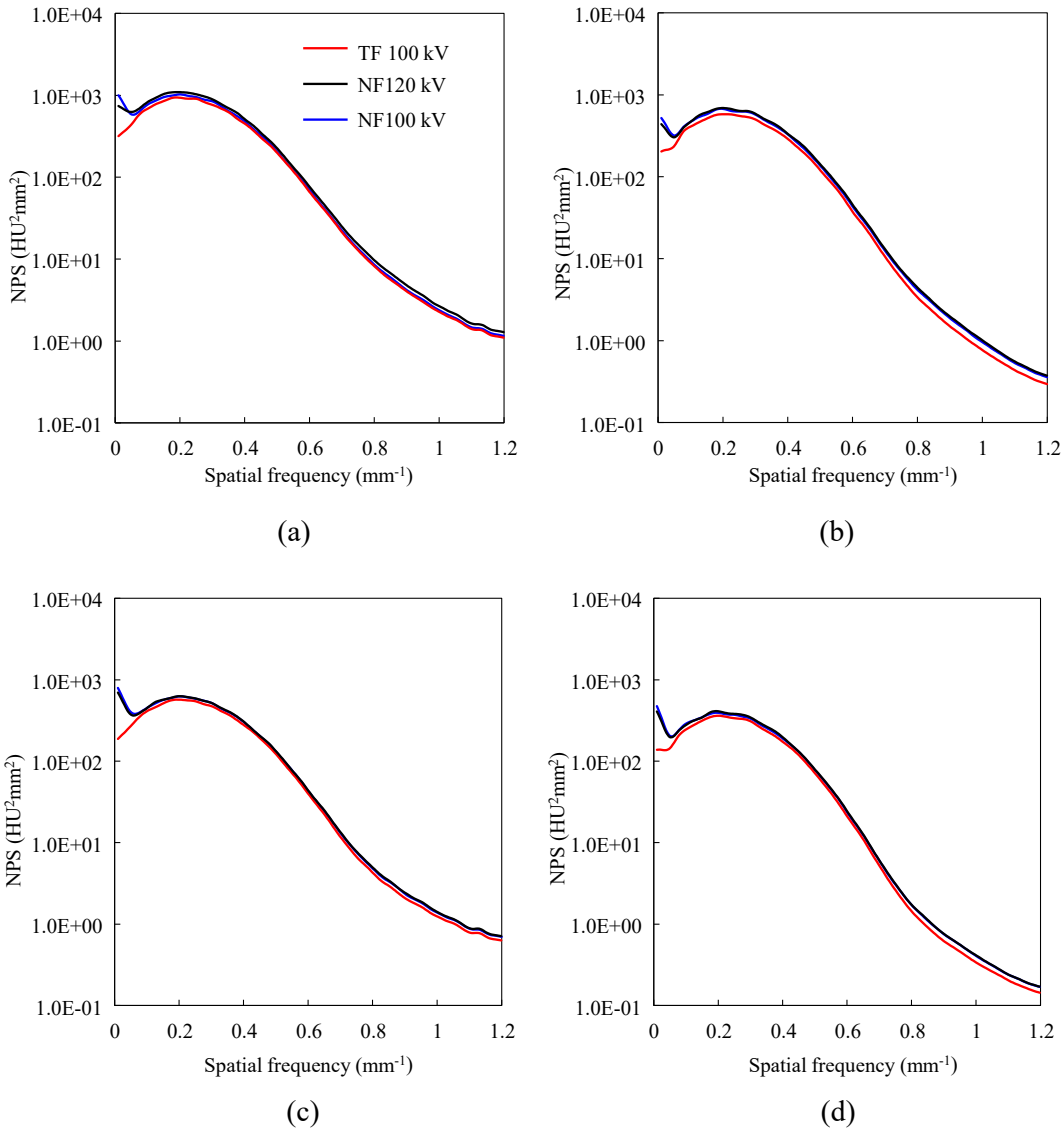

Fig. 3. NPS results of TF100kV, NF120kV, and NF100kV for (a) the AS and (b) the BS at 0.4 mGy; (c) the AS and (d) the BS at 0.8 mGy. The NPSs at the other doses (0.2, 0.6, and 1.0 mGy) exhibited similar tendencies.

Table 1
Results of area under the NPS curve for TF100kV, NF120kV, and NF100kV at dose levels of 0.2 to 1.0 mGy.

Area under the NPS curve (HU·mm^2)						
	Location corresponding to AS			Location corresponding to BS		
CTDIvol (mGy)	TF100kV	NF120kV	NF100kV	TF100kV	NF120kV	NF100kV
0.2	526.7	NA	602.4	357.6	NA	404.1
0.4	334.4	402.3	381.9	206.9	249.0	244.3
0.6	248.9	284.6	288.6	157.6	180.4	182.2
0.8	202.9	237.9	238.6	125.8	147.7	146.7
1.0	173.1	203.8	205.9	107.0	124.1	126.9

NA: not applicable.

Those based on NF100kV at 0.6 mGy were 25% at the AS and 24% at the BS.

CT images

Figs. 5 and 6 show typical CT images of TF100kV and NF120kV with window conditions for the mediastinum and the lung field, respectively. Corresponding to the NPS difference of 17% at both the AS and the BS, the image noise was somewhat lower with TF100kV than with NF120kV. In addition, although it is difficult in the lung regions, it is observed that the streak artifacts in the soft-tissue regions (arrows in Fig. 5) were reduced in the TF100kV compared with NF120kV.

Discussion

This study assessed imaging performance under low-dose conditions

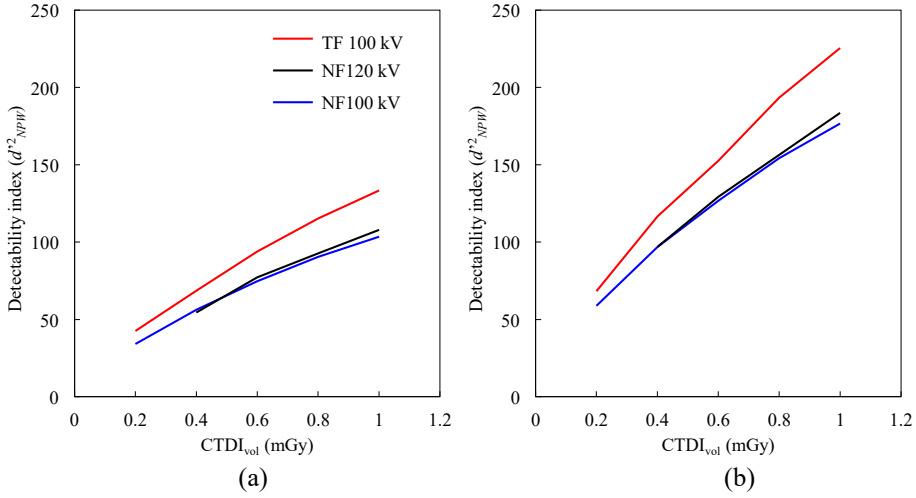

Fig. 4. d'^2_{NPW} of TF100kV, NF120kV, and NF100kV as a function of radiation dose for (a) the AS and (b) the BS.

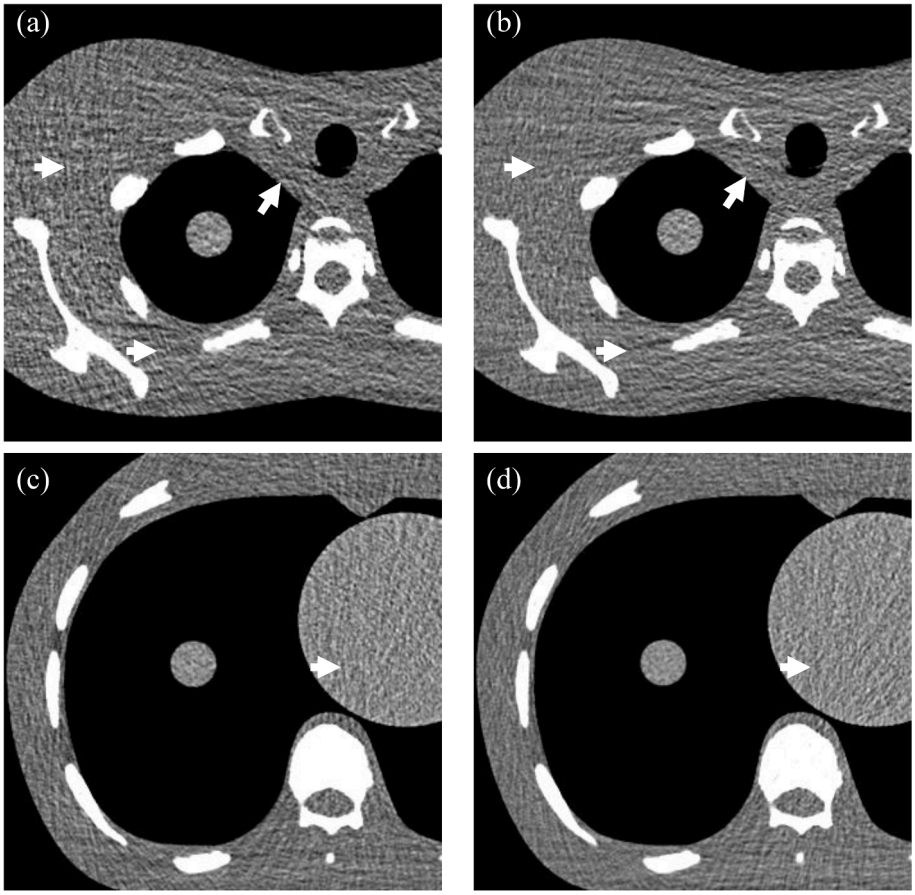

Fig. 5. Typical CT images obtained at 0.4 mGy with a window condition for the mediastinum (window width = 500 HU, window center = 30 HU) for (a) NF120kV and (b) TF100kV at the AS; (c) NF120kV and (d) TF100kV at the BS.

(0.2–1.0 mGy) with a TF (TF100kV) and without a TF (NF100kV and NF120kV), using d'_{NPW} measured at two locations in an anthropomorphic chest phantom. The CT number of the rod phantom decreased slightly (by 2–3 HU) with the TF, only at the BS; however, its effect on d'_{NPW} was negligible because the decrease in CT number was buried in the very high phantom contrast based on the background air (>1050 HU). Since the contrasts were almost identical and also the MTF was not altered by TF, we conclude that the difference in NPS is the main contributor to the changes in d'_{NPW}. It was found that the overall level of the NPS evaluated for the area under the NPS curve decreased roughly 15% with TF100kV compared with the non-TF cases. The NPS increases at low frequencies below 0.06 mm^{-1} present in the NPSs of NF100kV and NF120kV were not observed in the NPSs of TF100kV. This suggests that the TF effectively suppresses the streak artifacts frequently observed at low doses because of the better penetration of the X-ray hardened by the TF. As a result of these changes in NPS caused by the TF,

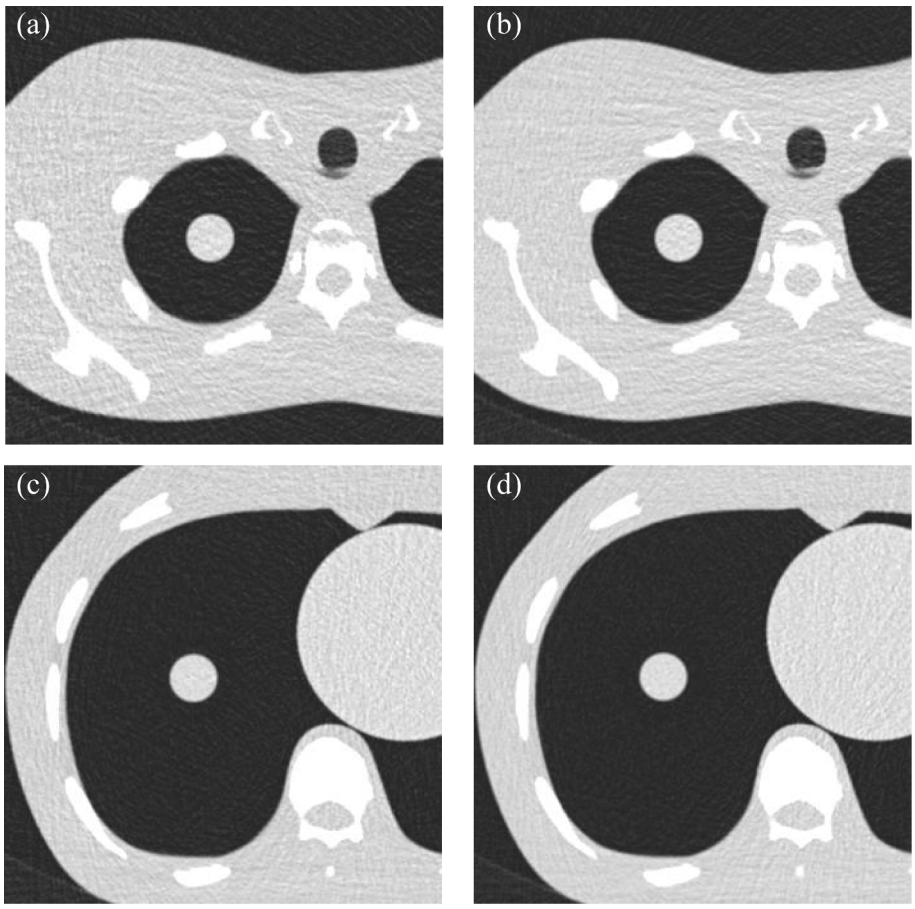

Fig. 6. Typical CT images obtained at 0.4 mGy with a window condition for the lung field (window width = 1500 HU, window center = − 500 HU) for (a) NF120kV and (b) TF100kV at the AS; (c) NF120kV and (d) TF100kV at the BS.

d'^2_{NPW} increased by 21.8–28.9% at the AS and 18.0–27.9% at the BS. We presume that the slightly higher d'^2_{NPW} improvement at the AS was observed because the effect on the streak artifact reduction was somewhat greater at the AS than at the BS. Based on our hypothesis that the rate of CT number change does not differ between the solid nodule and pure GGN, we can also presume that the improvement in d'_{NPW} by the TF for situations assuming the pure GGN is the same as that of the solid nodule. Consequently, with only the modest improvements in d'^2_{NPW} by the TF, we conclude that the potential dose reductions (22–25%) estimated in this study were notably lower than those expected by the results that have been reported so far.

The 100 kV for the TF was selected because it was reported in a document provided by the CT manufacturer that the mean energy of 100 kV with TF after passing through 30-cm water is similar to that of the standard 120 kV. Those energies of TF100kV and NF120kV are 79 and 81 keV, respectively [26]. Mean energies in the air of TF100kV and NF120kV in the manufacturer's report are 75 keV and 69 keV, respectively, which are nearly consistent with 76.0 and 64.2 keV reported in Ref. **2**. The 100 kV without TF (the mean energy of 58.7 keV reported in Ref. **2**) was additionally selected to examine the effect of TF at the same tube voltage. Tube voltages lower than 100 kV are practically difficult to use because the required tube currents may exceed the maximum one. Tube voltages higher than 100 kV are also practically difficult because not only the image contrast is unnecessarily decreased by the beam hardening by TF especially for bones, but also window setting to compensate for the contrast variations is not realistic for providing consistent CT images to many doctors.

Greffier et al. evaluated low-dose conditions (0.4–3.4 mGy) with and without a TF (TF at 100 kV and 150 kV, non-TF at 100 kV and 120 kV) using an ACR QA-phantom placed inside a body ring with a lateral diameter of 33 cm and an anterior-posterior diameter of 24 cm [2]. Although they also used d'_{NPW} in their assessment of low-dose conditions for chest CT, they used a phantom representing an adult abdomen; thus, the phantom attenuation was markedly different from (much higher than in) the present study of ours. Furthermore, they used an IR algorithm with a fixed strength. The percent improvement at 100 kV with a TF over the same voltage without a TF was reported to be 89% at 0.4 mGy, while our results showed notably lower improvements of 28.9% at maximum. We attribute this difference primarily to the difference in phantom attenuation and the use of IR. To properly assess potential dose reductions by a TF, it is essential to carefully choose a phantom appropriate for the purpose.

Some previously reported dose reductions by a TF in clinical low-dose chest CT are also difficult to compare with our results. As mentioned in Introduction, these studies evaluated image qualities with and without a TF between two different CT systems (second- and third-generation dual source CT systems) with different IR techniques and detector systems. Improved detector systems are effective in reducing image noise caused under low-dose conditions [27]; IR can offer comparable standard deviations (not the NPS) between high and low doses. It would be well presumable that these improvement factors also contributed significantly to the high dose reduction rates of nearly 90% reported in previous studies [3,4,6]. A study that compared a routine dose of 3.8 mGy without a TF and a low dose of 0.8 mGy with a TF, using one CT system, concluded that the routine dose with FBP is not significantly different from the low dose with IR in overall visual image quality [5]. Thus, in this situation, the dose reduction effect is not entirely attributable to the TF. Therefore, while potential dose

reductions in the previous studies featuring a TF are clinically relevant, the higher potentials were in fact achieved as a combined effect of a TF, a new detector and/or IR.

The present study has several limitations. First, no observer study was conducted to validate the potential dose reduction estimated by d'^{2}_{NPW}. Second, we used images reconstructed by FBP in order to evaluate the dose reduction performance of a TF. However, we should have also performed d'^{2}_{NPW} measurements with IR to evaluate the TF's performance to properly simulate the clinical conditions because IR is commonly used in clinical CT. Third, we used only a chest phantom mimicking an adult chest. Because of the beam hardening by a TF, there was a noticeable reduction in the contrast of bones [2]; in general, some contrast reductions are unavoidable with enhanced organs and vessels, although our preliminary literature survey produced no concrete evidence. Thus, it would be difficult to extend the application of TF to body parts other than the chest because the NPS improvement by a TF found in this study would be marred by contrast reductions. Nonetheless, it would be worthwhile to measure the effects on detectability index for other body parts. Fourth, although the tube voltage of 100 kV are commonly used in chest CT with the TF and tube voltages other than this voltage are difficult to use clinically as mentioned earlier, different energy level settings should be investigated to fully examine the effect of tin filter on the dose reduction.

Conclusion

When FBP images were used to evaluate the lone effect of the TF, the potential dose reduction at TF100kV, observed at locations corresponding to the apical and basal segments in a chest phantom, was estimated at 22–25% over NF120kV and NF100kV. This rate is significantly lower than those reported in previous studies that evaluated the combined effect of a TF, the CT system (particularly, detector), and IR in dose reduction performance.

Founding

This research did not receive any specific grant from funding agencies in the public, commercial, or not-for-profit sectors.

Declaration of Competing Interest

The authors declare that they have no known competing financial interests or personal relationships that could have appeared to influence the work reported in this paper.

References

[1] Brenner DJ, Hall EJ. Computed tomography: an increasing source of radiation exposure. N Engl J Med 2007;357:2277–84. https://doi.org/10.1056/nejmra072149.

[2] Greffier J, Pereira F, Hamard A, Addala T, Beregi JP, Frandon J. Effect of tin filter-based spectral shaping CT on image quality and radiation dose for routine use on ultralow-dose CT protocols: A phantom study. Diagn Interv Imaging 2020;101:373–81. https://doi.org/10.1016/j.diii.2020.01.002.

[3] Haubenreisser H, Meyer M, Sudarski S, Allmendinger T, Schoenberg OS, Henzler T. Unenhanced third-generation dual-source chest CT using a tin filter for spectral shaping at 100kVp. Eur J Radiol 2015;84:1608–13. https://doi.org/10.1016/j.ejrad.2015.04.018.

[4] Gordic S, Morsbach F, Schmidt B, Allmendinger T, Florh T, Husarik D, et al. Ultralow-dose chest computed tomography for pulmonary nodule detection: first performance evaluation of single energy scanning with spectral shaping. Invest Radiol 2014;49:465–73. https://doi.org/10.1097/rli.0000000000000037.

[5] Xu X, Sui X, Song L, Huang Y, Ge Y, Jin Z, et al. Feasibility of low-dose CT with spectral shaping and third-generation iterative reconstruction in evaluating interstitial lung diseases associated with connective tissue disease: an intra-individual comparison study. Eur Radiol 2019;29:4529–37. https://doi.org/10.1007/s00330-018-5969-y.

[6] Braun FM, Johnson TRC, Sommer WH, Thierfelder KM, Meinel FG. Chest CT using spectral filtration: radiation dose, image quality, and spectrum of clinical utility. Eur Radiol 2015;25:1598–606. https://doi.org/10.1007/s00330-014-3559-1.

[7] Vivier S, Deken V, Arous Y, Faivre JB, Duhamel A, Deschildre A, et al. Pediatric chest computed tomography at 100 kVp with tin filtration: comparison of image quality with 70-kVp imaging at comparable radiation dose. Pediatr Radiol 2020;50:188–98. https://doi.org/10.1007/s00247-019-04543-w.

[8] Bodelle B, Fischbach C, Booz C, Yel I, Frellesen C, Kaup M, et al. Single-energy pediatric chest computed tomography with spectral filtration at 100 kVp: effects on radiation parameters and image quality. Pediatr Radiol 2017;47:831–7. https://doi.org/10.1007/s00247-017-3813-1.

[9] Steidel J, Maier J, Sawall S, Kachelrieß M. Dose reduction potential in diagnostic single energy CT through patient-specific prefilters and a wider range of tube voltages. Med Phys 2022;49(1):93–106. https://doi.org/10.1002/mp.15355.

[10] Kawashima H, Ichikawa K, Hanaoka S, Matsubara K, Takata T. Relationship between size-specific dose estimates and image quality in computed tomography depending on patient size. J Appl Clin Med Phys 2018;19:246–51. https://doi.org/10.1002/acm2.12340.

[11] Samei E, Bakalyar D, Boedeker KL, Brady S, Fan J, Leng S, Myers KJ, Popescu LM, Giraldo JCR, Ranallo F, Solomon J, Vaishnav J, Wang J. Report No. 233 - Performance Evaluation of Computed Tomography Systems - The Report of AAPM Task Group 233 (2019). American Association of Physicists in Medicine. https://www.aapm.org/pubs/reports/detail.asp?docid=186 [accessed 21 December 2021].

[12] Richard S, Husarik DB, Yadava G, Murphy SN, Samei E. Towards task-based assessment of CT performance: System and object MTF across different reconstruction algorithms. Med Phys 2012;39:4115–22. https://doi.org/10.1118/1.4725171.

[13] Takata T, Ichikawa K, Mitsui W, Hayashi H, Minehiro K, Sakuta K, et al. Object shape dependency of in-plane resolution for iterative reconstruction of computed tomography. Phys Med 2017;33:146–51. https://doi.org/10.1016/j.ejmp.2017.01.001.

[14] Ichikawa K, Kawashima H, Shimada M, Adachi T, Takata T. A three-dimensional cross-directional bilateral filter for edge-preserving noise reduction of low-dose computed tomography images. Comput Biol Med 2019;111:103353. https://doi.org/10.1016/j.compbiomed.2019.103353.

[15] Kawashima H, Ichikawa K, Matsubara K, Nagata H, Takata T, Kobayashi K. Quality evaluation of image-based iterative reconstruction for CT: Comparison with hybrid iterative reconstruction. J Appl Clin Med Phys 2019;20:199–205. https://doi.org/10.1002/acm2.12597.

[16] Kawashima H, Ichikawa K, Takata T, Mitsui W, Ueta H, Yoneda N, et al. Performance of clinically available deep learning image reconstruction in computed tomography: a phantom study. J Med Imaging (Bellingham) 2020;7:063503. https://doi.org/10.1117/1.jmi.7.6.063503.

[17] Samei E, Richard S. Assessment of the dose reduction potential of a model-based iterative reconstruction algorithm using a task-based performance metrology. Med Phys 2015;42:314–23. https://doi.org/10.1118/1.4903899.

[18] Urikura A, Hara T, Ichikawa K, Nishimaru H, Hoshino T, Yoshida T, et al. Objective assessment of low-contrast computed tomography images with iterative reconstruction. Phys Med 2016;32:992–8. https://doi.org/10.1016/j.ejmp.2016.07.003.

[19] Loo L-N D, Doi K, Metz CE. A comparison of physical image quality indices and observer performance in the radiographic detection of nylon beads. Phys Med Biol 1984;29(7):837–56.

[20] Sharp P, Barber DC, Brown DG, Burgess AE, Metz CE, Myers KJ, Taylor CJ, Wagner RF, Brooks R, Hill CR, Kuhl DE, Smith MA, Wells P, Worthington B. ICRU Report 54: Medical Imaging - the Assessment of Image Quality; Appendix F: The Non-Prewhitening Matched Filter (NPWMF). Journal of the ICRU 1996:66–7. 10.1093%2Fjicru_os28.1.66.

[21] Sato K, Shidahara M, Goto M, Yanagawa I, Homma N, Mori I. Aliased noise in X-ray CT images and band-limiting processingas a preventive measure. Radiol Phys Technol 2015;8:178–92. https://doi.org/10.1007/s12194-015-0306-5.

[22] Nickoloff EL. Measurement of the PSF for a CT scanner: appropriate wire diameter and pixel size. Phys Med Biol 1988;33:149–55. https://doi.org/10.1088/0031-9155/33/1/014.

[23] Kawashima H, Ichikawa K, Takata T, Nagata H, Hoshika M, Akagi N. Technical Note: Performance comparison of ultra-high-resolution scan modes of two clinical computed tomography systems. Med Phys 2020;47:488–97. https://doi.org/10.1002/mp.13949.

[24] Xu DM, van der Zaag-Loonen HJ, Oudkerk M, Wang Y, Vliegenthart R, Scholten ET, et al. Smooth or attached solid indeterminate nodules detected at baseline CT screening in the NELSON study: cancer risk during 1 year of follow-up. Radiology 2009;250:264–72. https://doi.org/10.1148/radiol.2493070847.

[25] Li Q, Fan L, Cao ET, Li QC, Gu YF, Liu SY. Quantitative CT analysis of pulmonary pure ground-glass nodule predicts histological invasiveness. Eur J Radiol 2017;89:67–71. https://doi.org/10.1016/j.ejrad.2017.01.024.

[26] Woods M, Brehm M. White paper: Shaping the beam. Versatile filtration for unique diagnostic potential within Siemens Healthineers CT. Siemens AG, https://cdn0.scrvt.com/39b415fb07de4d9656c7b516d8e2d907/1800000006857523/27030c03dfe2/siemens-healthineers-ct-technologies-and-innovations-tin-filter-whitepaper_v2_1800000006857523.pdf [accessed 31 March 2022].

[27] Ulzheimer S, Freund J. White Paper: The Stellar Detector. Siemens AG, https://cdn0.scrvt.com/39b415fb07de4d9656c7b516d8e2d907/1800000003369873/c3565f4372f7/Computed-Tomography_Machine-Technology_Stellar-detector_Whitepaper_1800000003369873.pdf [accessed 21 December 2021].